

# *In vivo* imaging and low-coherence interferometry of organ of Corti vibration

## Fangyi Chen

Oregon Health and Science University  
Oregon Hearing Research Center  
3181 Southwest Sam Jackson Park Road, NRC04  
Portland, Oregon 97239-3098

## Niloy Choudhury

Oregon Health and Science University  
Biomedical Engineering  
CH13B, 3303 Southwest Bond Avenue  
Portland, Oregon 97239

## Jiefu Zheng

## Scott Matthews

Oregon Health and Science University  
Oregon Hearing Research Center  
3181 Southwest Sam Jackson Park Road, NRC04  
Portland, Oregon 97239-3098

## Alfred L. Nutall

Oregon Health and Science University  
Oregon Hearing Research Center  
3181 Southwest Sam Jackson Park Road, NRC04  
Portland, Oregon 97239-3098

and

Oregon Health and Science University  
Biomedical Engineering  
CH13B, 3303 Southwest Bond Avenue  
Portland, Oregon 97239

and

The University of Michigan  
Kresge Hearing Research Institute  
1301 East Ann Street  
Ann Arbor, Michigan 48109-0506

and

Shanghai Jiao Tong University  
Renji Hospital  
Department of Otolaryngology  
1954 Shanghai Huansan Road  
Shanghai, China

## Steven L. Jacques

Oregon Health and Science University  
Biomedical Engineering  
CH13B, 3303 Southwest Bond Avenue  
Portland, Oregon 97239

and

Oregon Health and Science University  
Dermatology  
CH13B, 3303 Southwest Bond Avenue  
Portland, Oregon 97239

E-mail: sjacques@bme.ogi.edu

## 1 Introduction

Current research in hearing is concerned with the mechanics of how sound waves propagate down the ribbon-shaped basilar membrane (BM), and how movement of the membrane imparts movement to the cellular and noncellular components

**Abstract.** An optical coherence tomography (OCT) system is built to acquire *in vivo* both images and vibration measurements of the organ of Corti of the guinea pig. The organ of Corti is viewed through a  $\sim 300\text{-}\mu\text{m}$ -diam hole in the bony wall of the cochlea at the scala tympani of the first cochlear turn. In imaging mode, the image is acquired as reflectance  $R(x, z)$ . In vibration mode, the basilar membrane (BM) or reticular lamina (RL) are selected by the investigator interactively from the  $R(x, z)$  image. Under software control, the system moves the scanning mirrors to bring the sensing volume of the measurement to the desired membrane location. *In vivo* images of the organ of Corti are presented, indicating reflectance signals from the BM, RL, tectorial membrane, and Reissner's membrane. The tunnel of Corti and the inner sulcus are also visible in the images. Vibrations of  $\pm 2$  and  $\pm 22$  nm are recorded in the BM in response to low and high sound levels at 14 kHz above a noise floor of 0.2 nm. © 2007 Society of Photo-Optical Instrumentation Engineers. [DOI: 10.1117/1.2717134]

Keywords: cochlea; vibration; optical coherence tomography; interferometry.

Paper 06168SSR received Jun. 23, 2006; revised manuscript received Dec. 28, 2006; accepted for publication Jan. 15, 2007; published online Apr. 12, 2007.

of the organ of Corti, which are attached to the BM. Critical vibration components are the BM, the hair cells, the reticular lamina (RL), and the gelatinous tectorial membrane (TM). The organ of Corti is a complex irregularly shaped structure that moves in a complex fashion when the BM vibrates, imparting a shear stress on the stereocilia of the hair cells that extend from the RL into or near the TM. Also, the outer hair cells of the organ are active elements, which can provide posi-

---

Address all correspondence to Steven Jacques, Biomedical Engineering/Dermatology, Oregon Health & Science Univ., Mail code: CH13B - 3303 SW Bond Avenue, Portland, OR 97239, United States of America; Tel: 503-418-9338; Fax: 503-418-9311; E-mail: sjacques@bme.ogi.edu

tive feedback to vibration of the organ, thereby increasing the resonance of that portion of the membrane to a particular frequency.

Our project is to use low-coherence interferometry to measure the amplitude and phase of the various components of the organ of Corti, especially the BM and RL. Documenting the amplitude and phase difference between the BM and RL would contribute information pertinent to the active mechanisms involved in the resonant response of the cochlear partition.

Our first report (Choudhury et al.<sup>1</sup>) demonstrated the use of a low-coherence interferometric system in an *ex vivo* preparation of an isolated cochlea from a guinea pig. The report showed the ability to measure 16-kHz vibrations in the 0.1 to 10-nm amplitude range with a noise floor of 0.040 nm. This report describes our first *in vivo* measurements on three animals. Images of the organ of Corti were obtained by optical coherence tomography (OCT). Vibration measurements were obtained by fixing the positions of the scan mirrors of the OCT system so that the measurement was localized on the BM or the RL.

The literature on interferometric measurements of organ of Corti movement has relied on systems that use lasers with long coherence lengths (e.g., the HeNe laser).<sup>2-10</sup> With long-coherence lasers, reflectances from various tissue structures in the  $\sim 100\text{-}\mu\text{m}$ -thick organ of Corti contribute to the detected interferometric signal and yield a complex signal not assignable to just the BM or RL membrane. The ability to use a high numerical aperture lens to achieve localized measurements is limited by the need to deliver the light through a small hole in the wall of the cochlea. To overcome this problem of localizing the measurement, investigators routinely introduce reflective beads that adhere to the BM and provide a strong reflectivity so that vibration of the bead dominates the interferometric signal. However, it is not practical to adhere beads to the other structures of the organ of Corti of the first turn, in particular the RL.

The low-coherence interferometric system is able to make measurements using the native reflectance of the tissues, without the use of reflective beads. The system can acquire a very localized measurement, since the coherence length of the broadband light source (a superluminescent diode) sets the axial resolution to  $\sim 10\ \mu\text{m}$ , even when using a low numerical aperture lens whose focus may extend over several  $100\ \mu\text{m}$ . The  $\sim 10\text{-}\mu\text{m}$  coherence gate acts as an effective 45-fs time gate that rejects scattered photons that arrive either before or after the time gate of collection. This time gate significantly reduces the background noise (i.e., the background speckle) due to multiply scattered light. In summary, three major advantages of low-coherence interferometry over traditional interferometers using light sources with long coherence lengths are: 1. measurements use native tissue reflectance and do not require reflective beads, 2. measurements are made on an isolated surface, such as the basilar membrane, while rejecting signals from other neighboring surfaces, such as the reticular lamina, and 3. the noise level is reduced, since noise from laser speckle and minor tissue fluctuations outside the coherence gate are rejected.

The use of low-coherence light also allows acquisition of images of the organ of Corti using the OCT method. While vibration measurement, not imaging, is the primary goal of

our work, the OCT image assists the adjustment of scanning mirrors to localize the vibration measurement on structures of interest, such as the basilar membrane and reticular lamina. Wong et al.<sup>11,12</sup> reported *in vivo* OCT images of the inner ear in a rat model, obtained through the bone. Recently, Hong and Freeman<sup>13</sup> reported the use of Doppler optical coherence microscopy to image an exposed gerbil cochlea, using a high numerical aperture lens, since there was no need to deliver the light through a small hole in the wall of the cochlea. Consequently, the images have rather high spatial resolution. This work demonstrates imaging through a hole in the cochlear wall to yield detailed *in vivo* images of the organ of Corti that show the BM, RL, tectorial membrane, tunnel of Corti, inner sulcus, and Reissner's membrane.

## 2 Materials and Methods

### 2.1 Animals

The cochleae of three deeply anesthetized guinea pigs were surgically exposed by resection of the overlying tissue, then a  $300\text{-}\mu\text{m}$ -diam hole in the basal-turn scala tympani of the cochlea was created. Sound was generated by a speaker and introduced via a closed sound field into the ear in a manner that was calibrated to yield a known acoustic power. The cochleae of these three guinea pigs were insensitive at the time of experimental measurements, and relatively loud sound pressures were used to achieve vibration amplitudes comparable to the vibrations of a sensitive ear responding to common sound levels. The procedures of this study were approved by the Animal Institutional Care and Use Committee of Oregon Health and Sciences University.

### 2.2 Optical System

An optical coherence tomography (OCT) system was assembled to provide a low-coherence interferometric imaging and vibration measurement system. When scanned as a classical OCT system, the system yielded an image of the organ of Corti based on photons reflected from the tissue. When the scanning mirrors were fixed, and the system's sensing was positioned on the BM or RL of the organ of Corti, the system served as a classic homodyne interferometer that could sense the movements of the selected membrane.

The basis of the system is the use of a broadband light source to yield a short coherence length, which allows for light reflected from the sample and reference arms to interfere only within a very limited spatial range of photon pathlength called the "coherence gate." In this system, the coherence gate was Gaussian shaped with a full-width half-maximum (FWHM) of  $\sim 10\ \mu\text{m}$  in water ( $9.6\ \mu\text{m}$ , measured by imaging a glass/water interface) along the  $z$  axis roughly perpendicular to the BM. Therefore, as the pathlength of the reference arm was modulated by a  $z$ -axis scanning galvo-mirror [see Fig. 1(c)], the coherence gate was moved axially within the sample. A second galvo-mirror provided for lateral  $x$ -axis scanning [see Fig. 1(b)]. The acquired image presented the reflectance in an  $x$ - $z$  plane,  $R(x, z)$ , with  $10\text{-}\mu\text{m}$  axial and  $\sim 20\text{-}\mu\text{m}$  lateral resolution.

The OCT system used a superluminescent diode as the light source (1310 center wavelength, 94-nm full-width half-max bandwidth,  $\sim 10\text{-mW}$  power, BWTek Incorporated,

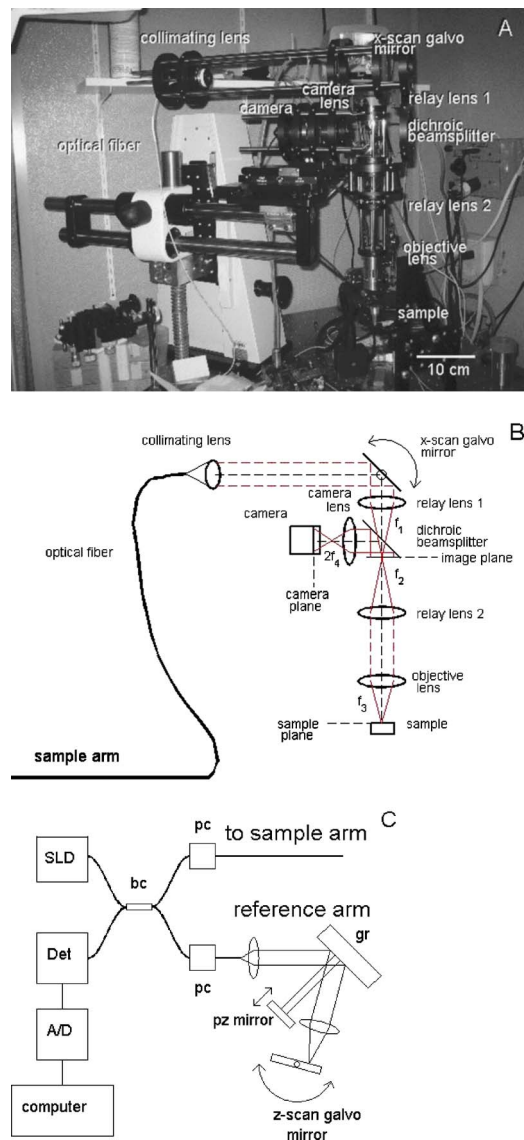


**Fig. 1** (a) Photograph of the experimental setup. (b) Schematic of the optics of the sample arm that views the tissue. An  $x$ -axis galvo-mirror scans laterally. A camera views the image of the tissue. (c) Schematic of the interferometer. The reference arm axially scans the coherence gate using the  $z$ -axis galvo-mirror ( $z$ -axis galvo) in a rapid scanning delay line. A piezo-driven mirror (PZ mirror) modulates the path-length of the delay line by 10 nm at 9 kHz to allow correction for the quadrature of the measurement. (SLD=superluminescent diode, bc=bridge coupler, pc=polarization controller, gr=grating, pz mirror=piezoelectric mirror, Det=diode detector, A/D=analog to digital converter.)

Newark, Delaware), delivering  $\sim 3$  mW to the sample. The experimental apparatus is shown in Fig. 1, which is a standard time-domain OCT system using a scanning phase delay line (following Rollins et al.<sup>14</sup>) in the reference arm to achieve longitudinal  $z$ -axis scanning and a galvo-mirror in the sample arm for lateral  $x$ -axis scanning. An additional piezo-driven mirror in the reference arm [see Fig. 1(c)] provided rapid 10-nm-amplitude  $z$ -axis modulation of the reference arm path-length to yield a modulated signal that aided the discrimination of the amplitude of the cochlear tissue vibration, despite

variation in the quadrature of the interferometric signal due to animal and system movements (discussed later in Sec. 2.22.). The signal arm of the OCT system delivered light via a single-mode optical fiber and a collimated lens assembly to yield a 4-mm-diam beam. This beam was reflected off a scanning galvo-mirror for  $x$ -axis scanning, passed through a pair of relay lenses (both 7.5-mm focal lengths, giving no change in beam size) that translated the angle of deflection off the galvo-mirror into an angle of entry into the objective lens. The objective lens (a single lens, 25-mm focal length, 25.4 mm diam) transformed the variable angle of entry of collimated light into a variable  $x$ -axis position of focus in the focal plane within the sample [labeled as “sample plane” in Fig. 1(b)]. The 4-mm-diam beam and 25-mm focal length specified a numerical aperture (NA) of 0.080, which yielded a focus with 143- $\mu\text{m}$  axial ( $z$ ) and  $\sim 20$ - $\mu\text{m}$  lateral ( $x$ ) dimensions (FWHM). The 10- $\mu\text{m}$  coherence gate restricted the axial response, so the final spatial response was 10- $\mu\text{m}$  axial, 20- $\mu\text{m}$  lateral.

The strength of reflected signal when the coherence gate was positioned on an object varied as the position of the object was varied axially, either exactly in the focus or outside the focus of the objective lens. This response function, the so-called “focus function,” had a FWHM of 143  $\mu\text{m}$  along the  $z$  axis, based on experiments not shown in which an oil-glass interface was translated to different axial positions, and images were acquired. Images of the organ of Corti were acquired with the focus function positioned on the organ, and hence the effect of the focus function was minor for the image of the organ of Corti. An image of the sample plane in the tissue occurred in the image plane located midway between the two relay lenses. A charge-coupled device (CCD) camera was located in the camera plane at two focal lengths from a lens that viewed the image plane via a dichroic filter serving as a beamsplitter, and hence viewed the sample plane in the tissue. This lens was located two focal lengths from the image plane, and the camera plane was two focal lengths from the lens. The focal lengths  $f_1$ ,  $f_2$ ,  $f_3$ , and  $f_4$  shown in Fig. 1(b) were 7.5, 7.5, 25, and 50 mm, respectively.

The primary purpose of the imaging mode was not to acquire the highest possible resolution image, but rather to image the organ of Corti sufficiently well to allow selection of the position of the BM or RL surfaces by the investigator via a custom user interface for vibration measurements. After acquisition of an image, the investigator would view the image on the computer screen and click the mouse on the desired tissue feature. The  $x$ - and  $z$ -scanning mirrors would then translate and stop, locking the coherence gate onto the selected location in the sample. The system was then ready for vibration measurements. The following two sections describe the *imaging mode* and *vibration mode* of operation in more detail.

### 2.2.1 Imaging mode

In imaging mode, the  $z$ -axis galvo-mirror in the reference arm and the  $x$ -axis galvo-mirror in the sample arm scanned the coherence gate over an  $x$ - $z$  plane of measurement, yielding an image  $R(x, z)$ . The  $z$ -axis galvo-mirror scanned the coherence gate over 500  $\mu\text{m}$  using a ramp voltage that repeated at 151 Hz with a scan velocity of 37.7 mm/s. The reflected

light was detected by a photodiode (AC coupled, bandpass filter=30 to 100 kHz, New Focus, San Jose, California), and acquired by a data acquisition card (16-bit A/D converter, 400-kHz sampling, scale set to  $\pm 0.5$  V, National Instruments Corporation, Austin, Texas). Software control was accomplished using the MatLab® programming environment (The MathWorks, Incorporated, Natick, Massachusetts).

The image was initially acquired as an oscillatory signal  $V(t)$  expressed in volts. A calibration factor, CALIB [V/W], related detected volts to detected optical power. The raw image is shown in Fig. 2(a) (left) as the interferometric signal that oscillates along the vertical time axis of acquisition during each axial scan as an oscillating voltage  $V(t)$ . The detected signal at one  $x$  position is shown in Fig. 2(b) and is expressed:

$$V(t) = \text{CALIB}[I_S + I_R + (2I_S I_R)^{1/2} \cos(4\pi vt/\lambda)], \quad (1)$$

where  $I_S$  and  $I_R$  are the reflected powers from the sample and reference arms, respectively,  $v[\mu\text{m}/\text{s}]$  is the velocity of axially scanning the coherence gate,  $t[\text{s}]$  is time, and  $\lambda[\mu\text{m}]$  is the wavelength. The axial position of the coherence gate within the tissue was  $z=vt$ , where  $z=0$  was some position a few 100  $\mu\text{m}$  above (i.e., external to) the organ of Corti. The difference in photon pathlengths between the sample arm and reference arm was  $\Delta L=2\Delta z$ . The detector was AC coupled to detect only the cosine term in Eq. (1). The frequency of the oscillatory signal was  $2v/\lambda=58$  kHz. The signal was digitally filtered by a 58-kHz Gaussian bandpass (10-kHz FWHM), and the envelope  $E(t)$  of the oscillatory signal was detected by a Hilbert transform. These operations are summarized as:

$$E(t) = (2I_S I_R)^{1/2} = \text{Hilbert}[\text{filter}(V(t))]. \quad (2)$$

The signal  $E(t)$  was converted to  $E(z)$  using  $z=vt$ . The reflected signal from the sample  $I_S(z)$  was:

$$I_S(z) = E(z)^2/(2I_R). \quad (3)$$

The signal was calibrated by also measuring the signal from a mineral oil-glass interface,  $I_{Sog}$ , which provided a specular reflectance of  $r_{og}=[(1.52-1.46)/(1.52+1.46)]^2=0.0044$ , and calculating the reflected signal  $R(z)$  as [shown in Fig. 2(b)]:

$$R(z) = r_{og}I_S(z)/I_{Sog}. \quad (4)$$

Figure 2(a) (right) shows the calibrated  $R(x,z)$  image. Figure 2(c) shows the calibrated  $R(z)$  axial scan at one  $x$  position. The value of  $I_{Sog}$  used in Eq. (4) for calibration was determined with the oil-glass interface position exactly on the center of the axial scan ( $z=250 \mu\text{m}$ ). Figure 2(c) has been corrected for the focus function.  $R(z) \leftarrow R(z)/F(z)$ , where  $F(z)=\exp[-(z-z_o)/w]^2$ ,  $z_o=250 \mu\text{m}$  in the figure,  $w=118 \mu\text{m}$ . This was a modest correction but explains why the oil-glass interface in Fig. 2(c), although not in the center of the  $z$  scan, exactly matches the expected value of  $r_{og}$ . The  $R$  signals from the air-glass and water-glass interfaces did not exactly match the expected specular values, labeled  $r_{ag}$  and  $r_{wg}$ , respectively, in Fig. 2(c), because these signals had saturated the detector. They were not even similar to each other

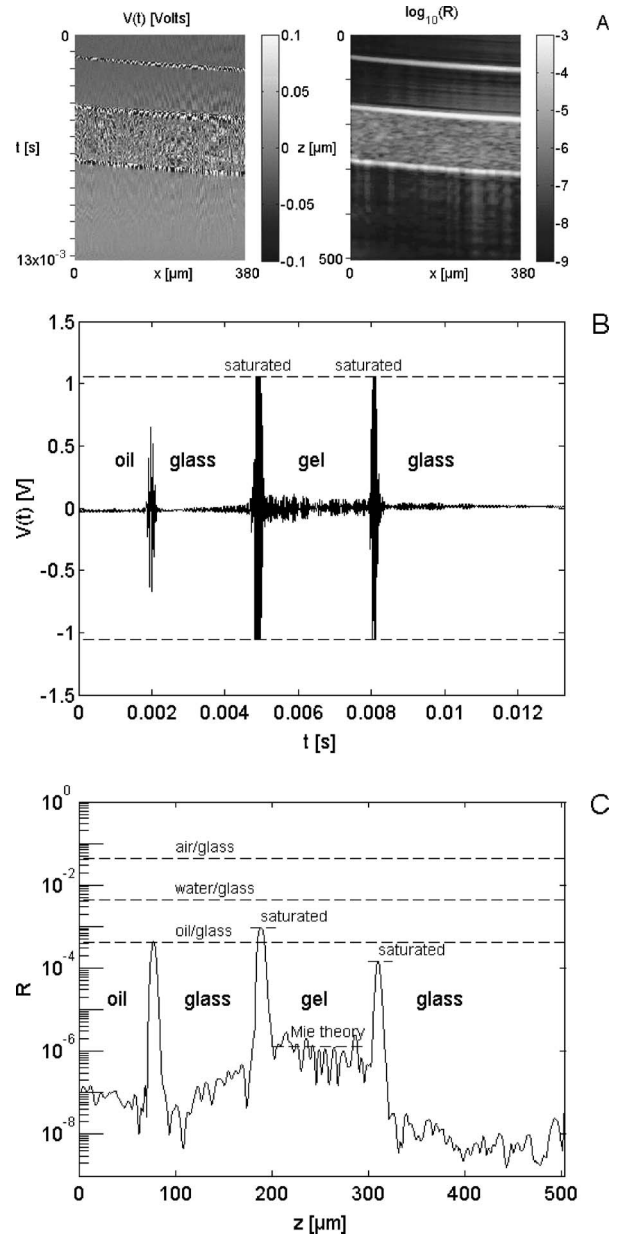


**Fig. 2** Image and calibration from oil/glass/microsphere-gel/glass layers. (a) On the left is the raw image acquired versus time at each  $x$  position, expressed as volts between  $\pm 0.1$  V. On the right is the calibrated image, based on the envelope of the raw image signal. From the top, the layers are the oil, glass coverslip, and gel with 0.1- $\mu\text{m}$ -diam polystyrene microspheres at 2.5% volume fraction, and a glass slide. (b) The raw signal is shown versus time at one  $x$  position, i.e., along a vertical line in (a) (left). The oil-glass interface is used for calibration. The glass-gel interfaces are saturated. (c) Calibrated axial scan of reflectance  $R(z)$ , i.e., along a vertical line in (a) (right). The prediction of the Mie theory for the microsphere gel is shown as a nearly horizontal dashed line between  $z=200$  to  $300 \mu\text{m}$ .

because the process of Eq. (2), when applied to saturated signals, was nonlinear.

The  $r_{og}$  from the oil-glass interface is comparable to the native reflectivities seen in tissues. By using an oil-glass interface, the gain of the electronics could be set so that the oil-glass calibration and all tissue measurements could be ob-

tained without saturation. The signals from water-glass and air-glass interfaces were allowed to saturate. The noise floor of the system was about 5 orders of magnitude (intensity scale) below the strongest signal in the OCT scan. So using the oil-glass calibration optimally positioned the dynamic range of measurements around the range of tissue reflectivities.

To provide a calibrated reference for comparison, a 2% agarose gel with 2.5% volume fraction of polystyrene microspheres (0.1  $\mu\text{m}$  diam) was prepared and imaged. The gel was characterized by collimated transmission measurements using an argon ion laser (488-nm wavelength), which indicated that the gel's measured optical scattering coefficient ( $\mu_s[\text{cm}^{-1}]$ ) matched the predictions of the Mie theory to within 20%. Using the Mie theory, the expected values of the scattering coefficient ( $\mu_s[\text{cm}^{-1}]$ ) and the anisotropy of scattering [ $g$  (dimensionless)] at the 1310-nm wavelength were 0.980  $\text{cm}^{-1}$  and 0.0185, respectively. The expected behavior of  $R(z)$  for the isotropic scattering from these microspheres was  $\rho e^{-\mu z}$ , where  $\rho$  (dimensionless) is a local reflectivity and  $\mu [\text{cm}^{-1}]$  is an apparent attenuation coefficient. The expected value of  $\rho$  was calculated as  $\rho = \mu_s L_{\text{cg}} b$ , where  $L_{\text{cg}} = 0.0096 \text{ cm}$  is the coherence gate length, and  $b = 0.00152$ . The fraction of light scattered by the tissue within the confocal volume that was collected within the coherence gate is  $\mu_s L_{\text{cg}}$ . The fraction of that scattered light backscattered into the collection solid angle of the objective lens is  $b$ . The expected value of  $\mu$  was calculated  $\mu = 2\mu_s$ , for the case of nearly isotropic scattering by small microspheres. The factor 2 accounts for the double path in/out of the tissue. The behavior of  $\rho e^{-\mu z}$  in the gel is shown as a nearly horizontal dashed line labeled "Mie theory" in Fig. 2(c).

Note that the calibration based on the oil-glass interface, and the calibration based on the polystyrene microsphere gel, were in good agreement. We suspect that the use of boundaries like an oil-glass interface is not always so reliable, since it may be affected by the angle of the interface relative to the optical axis and by the position of the interface relative to the focus of the objective lens. This concern was the motivation for exploring the use of a microsphere gel as the calibration standard. The speckle in the gel, however, was an unfortunate aspect of using the microsphere gel as a standard. Calibration of OCT images remains an on-going project in our laboratory.

### 2.2.2 Vibration mode

In vibration mode, a location in the image was selected by the investigator using a computer mouse, and the system controlled the galvo-mirrors to move the coherence gate to the selected  $x, z$  position and stopped the scanning. Now the system operated as an interferometer, and any movement of the tissue ( $\Delta z$ ) at that position was detected as a change in the detector voltage ( $\Delta V$ ), where  $\Delta V = \text{CALIB}(2I_S I_R)^{1/2} \cos(4\pi\Delta z/\lambda)$ .

A piezo-driven mirror in the reference arm [labeled "pz mirror" in Fig. 1(b)] allowed for the pathlength of the reference arm to be modulated as  $\Delta z_1 = A_1 \cos(2\pi f_1 t)$ ,  $A_1 = 10 \text{ nm}$ ,  $f_1 = 9 \text{ kHz}$ . The movement of the organ of Corti was driven by an acoustic signal (either 71- or 96-dB sound pressure level (SPL) at the tympanic membrane) to yield a vibration  $\Delta z_2 = A_2 \cos(2\pi f_2 t)$ ,  $f_2 = 14 \text{ kHz}$ . The experimen-

tally measured values of  $A_2$  were 2 and 22 nm for the 71- and 96-dB SPL pressures of these experiments in an insensitive ear. The acquired signal was:

$$V(t) = \text{CALIB} \cos[4\pi(\Delta z_1 + \Delta z_2)/\lambda + \Delta\phi],$$

$$V(t) = \text{CALIB} \cos\{4\pi[A_1 \cos(2\pi f_1 t + \Delta\phi_1) + A_2 \cos(2\pi f_2 t + \Delta\phi_2)]/\lambda\}, \quad (5)$$

where the term  $\Delta\phi$  denotes the phase difference between the sample and reference arms, which varied randomly over time due to movements of the animal and the system components. Hence, the strength of the vibration signal  $V(t)$  varied randomly over time, the so-called "quadrature" problem. To solve this problem, the signal was resolved in terms of two frequencies of oscillation, one due to the tissue vibration at  $f_1$  and the second due to the piezo mirror in the reference arm at  $f_2$ , characterized by a magnitude [ $M_1, M_2$  (a.u.)] and phase [ $\phi_1, \phi_2$  (radians)]:

$$V(t) = M_1 \cos(2\pi f_1 t + \phi_1) + M_2 \cos(2\pi f_2 t + \phi_2), \quad (6)$$

where  $M_1 = GA_1$  and  $M_2 = GA_2$ , with  $G$  denoting a randomly varying gain factor as the measurement moved in and out of quadrature. The gain factor  $G$  was also dependent on the strength of reflectance from the tissue, as described in Ref. 1. The detected phase of vibration ( $\phi_2$ ) of the sample was relative to the driving function of the acoustic signal. The ratio  $M_1/M_2$  canceled the gain factor  $G$  to yield  $A_1/A_2$ . In routine use, the  $M$  and  $\phi$  of the signals at frequencies  $f_1$  and  $f_2$  would be acquired by a lock-in amplifier, which we have done in some benchtop testing not shown here.

For this work a set of ten 0.1-s time traces of  $V(t)$  were acquired, and the average of the ten power spectra,  $P(f) = \text{fast Fourier transform (FFT)}[V(t)]$  was calculated.

$$P(f) = \text{FFT}[V(t)]. \quad (7)$$

The power  $P_1$  at  $f_1$  equaled  $M_1^2$  and was estimated as the mean of the  $9 \pm 0.5$ -kHz signal minus a baseline specified by the signals at 8 to 8.5 kHz and 9.5 to 10 kHz. The power  $P_2$  at  $f_2$  equaled  $M_2^2$  was estimated as the mean of the  $14 \pm 0.5$ -kHz signal minus a baseline specified by the signals at 10 to 11 kHz and 19 to 20 kHz. The ratio of acoustic power measurements was calculated:

$$S = P_2/P_1 = M_2^2/M_1^2 = G^2 A_2^2 / (G^2 A_1^2) = A_2^2/A_1^2, \quad (8)$$

which canceled any scaling factor associated with the method of estimating  $P_2$  and  $P_1$  and yielded the true value of  $S$ . Hence,  $S$  was proportional to the square of the tissue vibration amplitude  $A_2^2$ .

The ratio  $S$  was used to correct for the variation in the quadrature of the signal by allowing the common gain factor  $G^2$  to cancel to yield the ratio  $A_2^2/A_1^2$ . Since the  $A_2$  due to the piezo mirror vibration was a fixed value, the value of  $A_1$  was reliably specified. Hereafter in this work, the measurement signal  $S$  denotes the ratio  $P_2/P_1$ . Experiments not shown here of a vibrating surface (a piezo crystal) demonstrated the robust nature of this signal  $S$  despite variation in the quadrature of the signal.

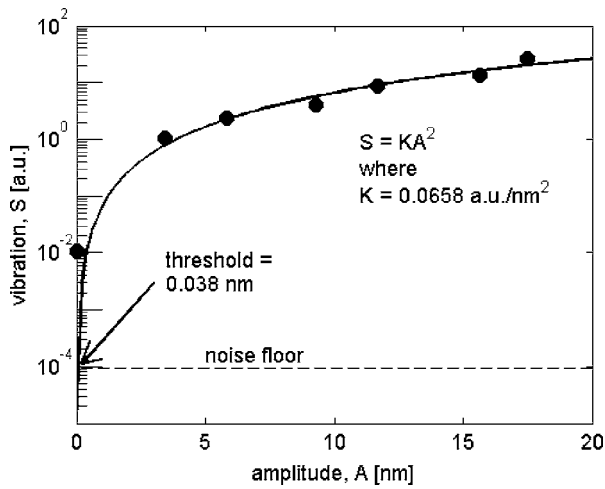


**Fig. 3** Calibration of the vibration measurement. The ratio of the raw vibration signals from the sample (12 kHz) and reference (9 kHz),  $S = M_s/M_r$ , is plotted versus the amplitude,  $A$  (nm), of vibration by a piezo crystal used for calibration. A calibration constant  $K$  was specified for the measurement. The noise floor of this experiment was  $\pm 0.038$ -nm vibration.

Calibration of the vibration signal  $S$  was accomplished by measuring the vibration of the front surface of a piezo (pz) crystal driven at 12 kHz at various driving voltages ( $V_{pz}$ ). The calibration used the same method of estimating  $P_1$  and  $P_2$  that was used for the tissue measurements. The detected signal  $S$  was related to the square of the amplitude of vibration ( $A^2$ ) as a function of driving voltage ( $V_{pz}$ ) according to the expression:

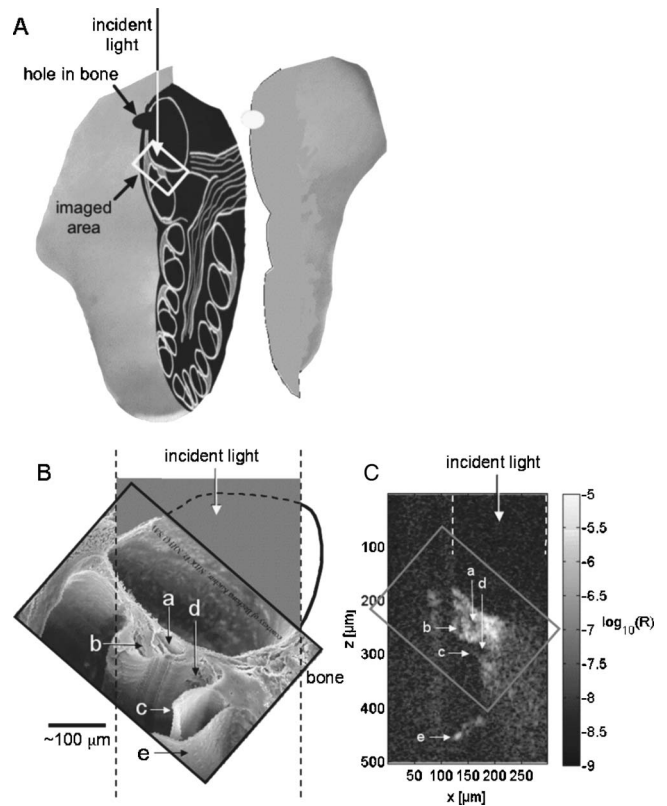
$$S = KA^2 = KC_{pz} V_{pz}^2 \quad (9)$$

The calibration constant  $C_{pz}$  [nm/ $V_{pz}$ ], such that  $A = C_{pz} V_{pz}$ , was determined using a commercially available interferometric system. The calibration constant  $K$  [ $V/nm^2$ ] was determined by plotting the  $S$  data versus the  $A$  specified by the choice of  $V_{pz}$ . The data are shown in Fig. 3 and conforms to  $S = KA^2$ , which indicated that  $K = 0.0658$  V/ $nm^2$ . Each vibration measurement  $S$  was routinely converted into amplitude of vibration  $A$  by the expression:

$$A = (S/K)^{1/2} \quad (10)$$

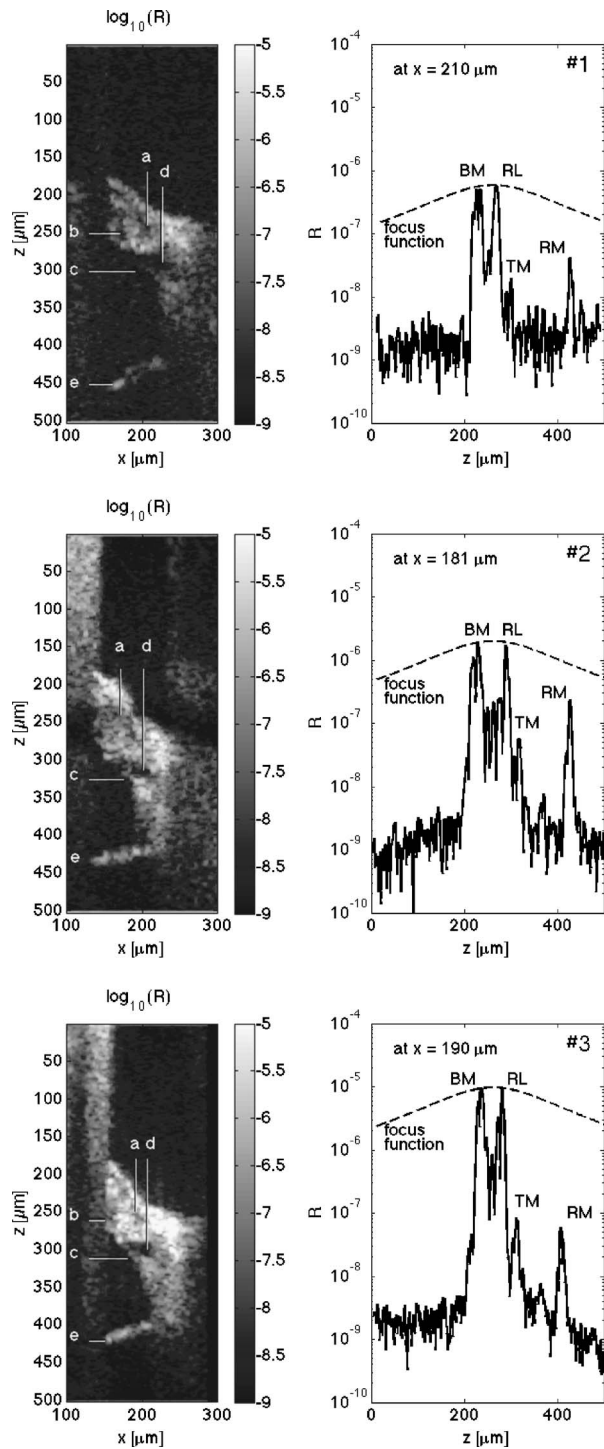
### 3 Results

*In vivo* OCT images of the organ of Corti were obtained in three guinea pigs while viewing through a 300- $\mu$ m-diam hole in the bone of the cochlea. Figure 4(a) shows a macroscopic schematic of the cochlea, illustrating how the objective lens delivered and collected light through the hole in the bone. Figure 4(b) shows a scanning electron microscope picture of the organ of Corti<sup>15</sup> that has been rotated to depict the geometry of light delivery and collection. Figure 4 shows the corresponding OCT image. Common landmarks seen in both Figs. 4(b) and 4(c) are a. the tunnel of Corti, b. Nuel's space, c. the tectorial membrane, d. the inner sulcus, and e. Reissner's membrane.



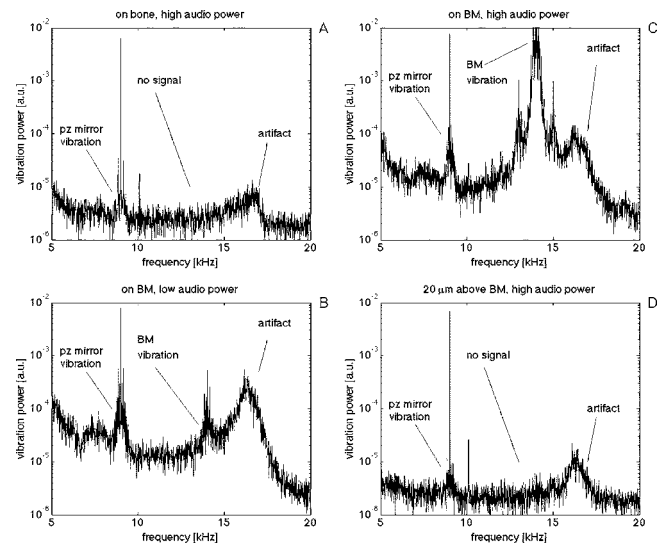
**Fig. 4** Imaging the organ of Corti. (a) The imaging was accomplished by delivery and collection of light through a small 300- $\mu$ m-diam hole in the cochlear bone. The organ of Corti is located within the rectangle showing the imaging area. (b) The light delivered through the hole in the bone impinged on part of the organ of Corti. An SEM image<sup>14</sup> has been rotated to indicate the orientation of the organ of Corti. Landmarks indicated are [a] tunnel of Corti, [b] Nuel's space, [c] tectorial membrane, [d] inner sulcus, and [e] Reissner's membrane. (c) The first *in vivo* OCT image of the organ of Corti. The same landmarks are indicated. The grayscale of the image indicates the reflectance ( $R$ ) expressed as  $\log_{10}(R)$ .

Figure 5 shows the calibrated OCT images,  $R(x, z)$ , and an axial scan at one  $x$  position,  $R(z)$ , for the three guinea pigs measured. The images show most of the organ of Corti, although the narrow view through the hole in the bone caused a portion of the organ of Corti to be cut off. The locations of the landmarks mentioned before are indicated. The axial scan  $R(z)$  shows the signals from the BM, reticular lamina (RL), tectorial membrane (TM), and Reissner's membrane (RM). All can be visualized above the background signal with signal-to-noise ratios of 1000, 1000, 10, and 100 for the BM, RL, TM, and RM, respectively. The noise floor is lower in these axial scans than in the microsphere/gel experiments of Fig. 2(c), because the noise floor is proportional to the strongest signal in the field of view and the glass/gel interface presented a strong signal. The dashed lines show the focus function that describes the responsivity of the system as a function of position relative to the depth position of the focus of the lens. In Figs. 2(a)–2(c), the focus of the lens was positioned onto the organ of Corti. The data are not yet normalized by the focus function, which is the next step that would yield calibrated data over the entire axial range of the scan.



**Fig. 5** Images and axial scans of organ of Corti for three guinea pigs (1, 2, and 3). On the left is the OCT image. The landmarks of Fig. 4 are indicated. On the right is an axial scan  $R(z)$  along one  $x$  position. The signals from the basal membrane (BM), reticular lamina (RL), tectorial membrane (TM), and Reissner's membrane (RM) are indicated. The dashed line indicates the experimentally determined focus function centered onto the organ of Corti.

Note that there is some variation in the strength of signal from the organ of Corti for these three animals. These are our first three animals ever imaged by OCT *in vivo*, and we do not have an explanation for the disagreement. We continue to ob-



**Fig. 6** The vibration measurements from animal 3, expressed as the raw data of vibration power spectrum ( $P$ , arbitrary units) versus frequency of acoustic energy delivered to the animal. The piezo mirror vibrated at 9 kHz and served as a reference. The acoustic vibration delivered to the animal was 14 kHz. (a) High-power measurement was located on the bone lateral to the basal membrane (BM). (b) Low-power measurement on the BM. (c) High-power measurement on the BM. (d) High-power measurement was located 20  $\mu\text{m}$  above the BM in the fluid.

serve variation in reflected signal in our current studies, even when translating longitudinally along the cochlear membrane in one particular animal. Our previous report had cited values of  $8 \times 10^{-5}$  reflectance for the BM and RL in an *ex vivo* preparation, comparable to animal 3. The signal to noise, i.e., the peak reflected signal from the organ of Corti relative to the

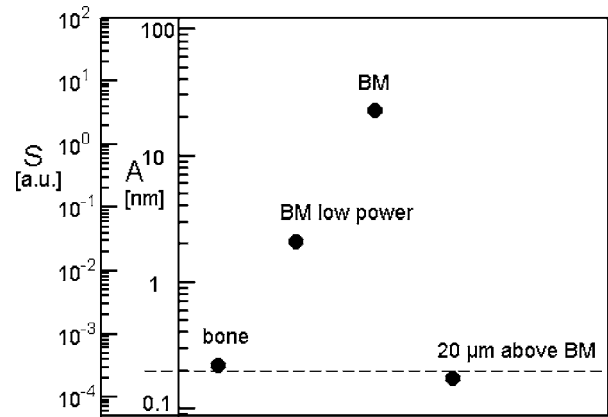


**Fig. 7** Vibration measurement  $S$  and amplitude  $A$  for the four sites measured (see Fig. 6). The noise floor was about 0.2-nm amplitude associated with the lack of signal from the bone and from the fluid 20  $\mu\text{m}$  above the BM. The BM showed a  $\pm 22$ -nm amplitude of vibration. These three measurements were stimulated by a high-power sound wave (96-dB SPL). The BM signal stimulated by a low-power sound wave (71-dB SPL) yielded  $\pm 2$ -nm amplitude of vibration. In these initial animal experiments, the ear was insensitive and vibrations were induced by high sound power levels. In the sensitive ear, vibrations of 2 and 22 nm would be induced by conversational levels and high environmental noise levels of sound, respectively.

**Table 1** Vibration measurements on organ of Corti in guinea pig 3. Sites were: 1. on bone lateral to basal membrane (BM), 2. on BM using low power, 3. on BM using high power, and 4. focused 20  $\mu\text{m}$  above the BM in the overlying fluid. Low and high power were 71- and 96-dB SPL, respectively, delivered to the ear at 14 kHz. The raw measurements in arbitrary units,  $M_r$  and  $M_s$ , for the 9-kHz piezo-mirror-induced reference and 14-kHz sound-induced signal, were acquired from the average of ten acoustic spectra, each acquired by FFT of a 100-ms time trace of signal. The ratio  $S=M_s/M_r$  was converted into amplitude of vibration  $A$  (nm).

Site	Power	$M_r$ [a.u.]	$M_s$ [a.u.]	$S=M_s/M_r$	$A=(S/K)^{1/2}$ (nm)
On bone	High	$0.0647 \times 10^{-3}$	$0.021 \times 10^{-5}$	0.0032	0.222
On BM	Low	$0.120 \times 10^{-3}$	$3.55 \times 10^{-5}$	0.296	2.12
On BM	High	$0.0886 \times 10^{-3}$	$300 \times 10^{-5}$	33.9	22.7
20 $\mu\text{m}$ off BM	High	$0.0686 \times 10^{-3}$	$0.014 \times 10^{-5}$	0.00200	0.174

noise floor, is about 1000:1 (30 dB), which is comparable to the signal to noise in the image reported by Hong and Freeman<sup>13</sup> using Doppler optical coherence microscopy.

Figure 6 shows the vibration signals from the organ of Corti expressed as the frequency spectrum of the signal  $V(t)$  of Eq. (6) while delivering acoustic waves to the ear at 14 kHz at high power (96-dB SPL or 1.3 Pa) [except Fig. 6(b), which used 71-dB SPL or 0.073 Pa]. Figure 6(a) shows the signal when the measurement was localized on the bone to the side of the organ of Corti. There is no signal at 14 kHz. The 9-kHz signal from the PZ mirror is seen. Also, there is an artifact at about 17 kHz, which we have subsequently shown to be due to jitter in the galvo-mirrors when held fixed by the active electronics of the mirror controller. Figure 6(b) shows the signal when the measurement was localized on the BM, and the low-power acoustic signal was administered. The 14-kHz frequency of vibration appears with a signal-to-noise ratio of 10. Figure 6(c) shows the signal from the BM when the high-power acoustic signal was delivered to the ear. The BM vibration is strongly evident, with a signal-to-noise ratio of 100. There are side bands to the BM vibration, the origin of which is not yet known, so we are re-examining the characteristics of the speaker system when driven at high-power levels. Figure 6(d) shows the measurement when the coherence gate was centered on the BM but retracted axially 20  $\mu\text{m}$  away from the BM. The vibration signal disappeared, illustrating the axial sectioning that the low-coherence interferometer achieves.

Figure 7 plots the values of amplitude for these four sites: high power on the bone, low power on the BM, high power on the BM, and high power 20  $\mu\text{m}$  above the BM. The values of amplitude cited for the “on bone” and “20  $\mu\text{m}$  above BM” measurements essentially demonstrated a practical noise floor of 0.2-nm amplitude obtained *in vivo*. This noise is greater than the 0.038-nm noise obtained in the calibration experiments (Fig. 3). Table 1 summarizes the quantitative values obtained from the vibration measurements in Fig. 6. The values of  $M_1$  and  $M_2$  in arbitrary units, the ratio  $S$ , and the amplitude  $A$  are listed for each of the four sites measured in animal 3.

## 4 Discussion

Wong et al.<sup>11,12</sup> have demonstrated the ability to obtain OCT images of the inner ear directly through the cochlea bone of an intact rat. Our previous report<sup>1</sup> demonstrated the ability to both image using OCT and measure vibration of the BM and RL using low-coherence interferometry. Hong and Freeman<sup>13</sup> report on the use of Doppler optical coherence microscopy to measure an exposed gerbil cochlea *in vitro*. This report presents the first *in vivo* vibration measurements in an animal model using low-coherence interferometry. The strengths of reflectance from the various structures of the cochlea (BM, RL, TM, and RM) shown in Fig. 4 suggest that future work could explore movements of all these structures.

The significance of this work is to achieve independent measurements of the BM and RL without cross talk. There are current issues regarding the role of active elements in the hair cells of the organ of Corti, which introduces resonance into the auditory response of the cochlear membrane at each particular position along its length. Measurements of the relative amplitude and phase of the BM and RL vibrations would contribute to this area of investigation. Our goal is to implement a two-channel interferometer that simultaneously measures both the BM and RL vibrations. This work describes a single channel system that demonstrates the feasibility of using low-coherence interferometry to make such vibration measurements on the BM using native reflectance, without the need for reflective beads.

### Acknowledgments

This work was supported by the National Institutes of Health, primarily NIDCD R01-DC006273 with partial support from NIDCD R01-DC00141 and NIDCD P30-DC005983.

### References

1. N. Choudhury, G. Song, F. Chen, S. Matthews, T. Tschinkel, J. Zhen, S. L. Jacques, and A. L. Nuttall, “Low coherence interferometry of the cochlear partition,” *Hear. Res.* **220**(1,2), 1–9 (2006).
2. A. L. Nuttall, D. F. Dolan, and G. Avinash, “Laser doppler velocimetry of basilar membrane vibration,” *Hear. Res.* **51**, 203–213 (1991).
3. N. P. Cooper, “An improved heterodyne laser interferometer for use in studies of cochlear mechanics,” *J. Neurosci. Methods* **88**, 93–102 (1999).

4. N. P. Cooper, "Vibration of beads placed on the basilar membrane in the basal turn of the cochlea," *J. Acoust. Soc. Am.* **106**, L59–L64 (1999).
5. S. M. Khanna, "Homodyne interferometer for basilar membrane vibration measurements," *Hear. Res.* **23**, 9–26 (1986).
6. E. Dalhoff, R. Gartner, H. Zenner, H. J. Tiziani, and A. W. Gummer, "Remarks about the depth resolution of heterodyne interferometers in cochlear investigations," *J. Acoust. Soc. Am.* **110**, 1725–1728 (2001).
7. A. L. Nuttall, D. F. Dolan, and G. Avinash, "Laser doppler velocimetry of basilar membrane vibration," *Hear. Res.* **51**, 203–213 (1991).
8. T. Ren and A. L. Nuttall, "Basilar membrane vibration in the basal turn of the sensitive gerbil cochlea," *Hear. Res.* **151**, 48–60 (2001).
9. T. Ren and A. L. Nuttall, "Recording depth of the heterodyne laser interferometer for cochlear vibration measurement," *J. Acoust. Soc. Am.* **109**, 826–829 (2001).
10. O. L. de la Rochefoucauld, S. M. Khanna, and E. S. Olson, "Recording depth and signal competition in heterodyne interferometry," *J. Acoust. Soc. Am.* **117**, 1267–1284 (2005).
11. B. J. Wong, J. F. de Boer, B. H. Park, Z. Chen, and J. S. Nelson, "Optical coherence tomography of the rat cochlea," *J. Biomed. Opt.* **5**(4), 367–370 (2000).
12. B. J. Wong, Y. Zhao, M. Yamaguchi, N. Nassif, Z. Chen, and J. F. De Boer, "Imaging the internal structure of the rat cochlea using optical coherence tomography at 0.827 micron and 1.3 micron," *Otolaryngol.-Head Neck Surg.* **130**(4), 458 (2004).
13. S. S. Hong and D. M. Freeman, "Doppler optical coherence microscopy for studies of cochlear mechanics," *J. Biomed. Opt.* **11**(5), 054014 (2006).
14. A. M. Rollins, M. D. Kulkarni, S. Yazdanfar, R. Ung-Arunyawee, and J. A. Izatt, "In vivo video rate optical coherence tomography," *Opt. Express* **3**, 219–229 (1998).
15. B. Kachar, NIDICD National Institutes of Health, see <http://www.vimm.it/cochlea/becharabw.jpg>.